

# Shape Induced Symmetry in Self-Assembled Mesocrystals of Iron Oxide Nanocubes

Sabrina Disch,<sup>1,†</sup> Erik Wetterskog,<sup>1,‡</sup> Raphaël P. Hermann,<sup>1,§</sup> German Salazar-Alvarez,<sup>‡</sup> Peter Busch,<sup>†</sup> Thomas Brückel,<sup>\*,†</sup> Lennart Bergström,<sup>\*,‡</sup> and Saeed Kamali<sup>||,¶</sup>

<sup>†</sup>Jülich Centre for Neutron Science JCNS and Peter Grünberg Institut PGI, JARA-FIT, Forschungszentrum Jülich, 52425 Jülich, Germany

<sup>‡</sup>Department of Materials and Environmental Chemistry, Arrhenius Laboratory, Stockholm University, 10691 Stockholm, Sweden

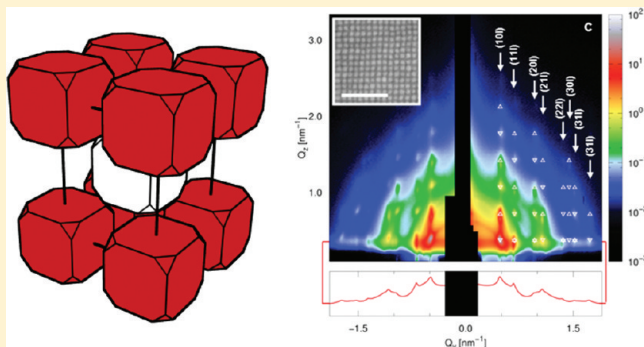
<sup>§</sup>Faculty of Science, University of Liège, B-4000 Liège, Belgium

<sup>||</sup>Japan Synchrotron Radiation Research Institute (JASRI), Spring-8, Sayo Hyogo 679-5198, Japan

**S** Supporting Information

**ABSTRACT:** Grazing incidence small-angle scattering and electron microscopy have been used to show for the first time that nonspherical nanoparticles can assemble into highly ordered body-centered tetragonal mesocrystals. Energy models accounting for the directionality and magnitude of the van der Waals and dipolar interactions as a function of the degree of truncation of the nanocubes illustrated the importance of the directional dipolar forces for the formation of the initial nanocube clusters and the dominance of the van der Waals multibody interactions in the dense packed arrays.

**KEYWORDS:** Nanoparticles, self-assembly, structure, GISAXS, iron oxide, particle interactions



Self-assembly of molecules and nanoparticles into tailored structures is a promising strategy for production and design of materials with new functions.<sup>1–4</sup> The spontaneous organization of the nanoscale building blocks into periodically packed structures is controlled by thermodynamic constraints and specific boundary conditions resulting in systems that commonly span a rich energy landscape.<sup>2,5</sup> Modulation of the particle interactions has a pivotal influence on the formed structures and the quality of nanocrystal mesocrystals.<sup>6–8</sup> Tuning the magnitude and directionality of the interparticle forces between, e.g., dipolar nanoparticles by applying electrical or magnetic fields may also have a profound effect on the assembly process and the resulting structures of the nanoparticle mesocrystals.<sup>9–13</sup>

The early work on self-assembly of nanoparticles focused on spheres, with hexagonally packed arrays being produced from monodisperse spheres<sup>14,15</sup> and more recently nanoparticle arrays with complex structures by mixing monodisperse spheres of different sizes.<sup>16–20</sup> Much less experimental work has been reported on the design of suitable conditions for formation of ordered arrays and full characterization of the (three-dimensional) structures formed from nonspherical objects.<sup>21–23</sup>

Here, we show how superparamagnetic iron oxide nanocubes with a well-defined shape and size can be assembled into well-ordered arrays and how the three-dimensional structure can be determined by a combination of grazing incidence small-angle scattering (GISAXS) and electron microscopy. We demonstrate how a small deviation from a perfect cubic geometry of the

nanoparticle building blocks can dictate the symmetry of the array and show for the first time that nonspherical nanoparticles can assemble into a highly ordered body-centered tetragonal structure. Energy models that account for the directionality and magnitude of the van der Waals and dipolar interactions as a function of the degree of truncation of the nanocubes were used to evaluate the importance of the directional dipolar forces in the self-assembly process and to predict the occurrence of simple cubic and body-centered tetragonal mesocrystal structures.

Iron oxide nanocrystals have attracted much interest for a range of applications because of the combination of tunable magnetic properties and controllable surface properties.<sup>24–28</sup> The oleic acid capped nanocrystals were prepared by a modified nonhydrolytic synthesis approach,<sup>9,25</sup> purified into a nanoparticle paste, and dispersed in toluene to a concentration of about  $10^{14}$  particles/mL (see Supporting Information for details). Germanium wafers were cleaned by sonication in toluene, followed by ethyl acetate and ethanol (30 min each). Fast evaporation of the carrier solvent was achieved by spin-coating an excess amount of toluene dispersion, at 1000 rpm for 20 s. Evaporation was slowed down (1–2 h) by depositing  $\sim 0.1$  mL dispersion ( $4.5 \times 10^{14}$  particles/mL) on a  $\sim 2$  cm<sup>2</sup> dry germanium substrate and then placing it in a closed Petri dish with a

**Received:** January 12, 2011

**Revised:** February 8, 2011

**Published:** March 09, 2011

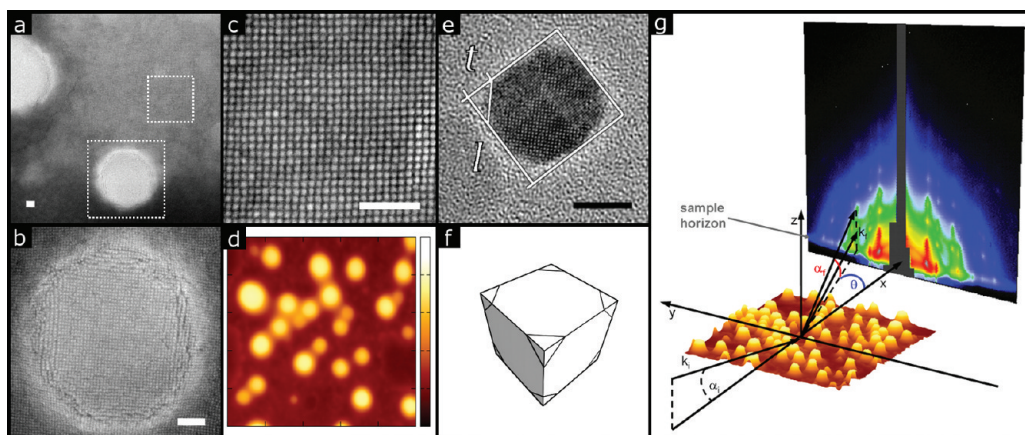


**Figure 1.** Characteristics of iron oxide nanocube mesocrystals, the nanocubes, and schematics of the GISAXS measurement and the obtained scattering pattern. (a–c) Scanning electron microscopy images of the (a) global and (b, c) detailed structures of the iron oxide nanocubes on Ge substrate indicated by the dashed squares; (b) mesocrystal embedded in (a); (c) monolayer of ordered nanocubes. Scale bars represent 100 nm. (d) Atomic force microscopy image of a  $10 \mu\text{m} \times 10 \mu\text{m}$  area of the same sample (z-range 500 nm). (e) High-resolution TEM photograph of the as-synthesized nanocubes and (f) schematic of the truncated cube. Note that the lattice fringes corresponding to (400) and (220) reflections (0.20 and 0.29 nm) are parallel and  $45^\circ$  to the cube edge, respectively. The truncation length,  $t$ , along the edge length,  $l$ , of the cube is shown. The scale bar corresponds to 5 nm. (g) Geometry of a typical GISAXS setup. The schematic shows the incoming beam with wavevector  $k_i$  at an angle  $\alpha_i$  to the sample surface. The arrangement of the nanoparticles gives rise to scattering with a wavevector  $k_f$  and scattering angles  $\theta$  inside the film plane and  $\alpha_f$  along the film normal.

diameter of 6–12 nm. With addition of a small reservoir of toluene (3–4 mL), the evaporation rate was further diminished. Applying a static field of  $\sim 30$  mT perpendicular to the wafer produced highly ordered mesocrystals. Transmission electron microscopy (TEM) images and selected area electron diffraction (SAED) patterns of the nanocrystals were acquired using a JEOL JEM-3010 microscope equipped with a LaB<sub>6</sub> filament operated at 300 kV ( $C_s = 0.6$  mm, point resolution = 0.17 nm). Scanning electron microscopy (SEM) images were obtained using a LEO 1550 SEM at 20 keV. Atomic force microscopy (AFM) measurements were carried out at ambient temperatures with an Agilent 5400 AFM. The instrument was operated in noncontact (AC) mode using a cantilever with a nominal spring constant of  $40 \text{ N m}^{-1}$ . Small-angle X-ray scattering (SAXS) was performed on dilute nanoparticle dispersions in toluene at the B1 beamline of the DORIS synchrotron at HASYLAB/DESY. The incident wavelength was 1.03 Å, and the detector distances were 0.93 and 3.63 m. The scattering recorded on a Pilatus 300K detector was averaged circularly (See Supporting Information). GISAXS measurements on the deposited superlattices were performed at the ID01 beamline of the ESRF. A CCD detector was set up at a distance of 0.519 m from the sample. The incident wavelength was set to 1.75 Å, and the incident angle of the primary beam was varied between  $0.30$  and  $0.60^\circ$ . The critical angle of the samples at the chosen conditions is  $0.125^\circ$ . A description of the data treatment is given in the Supporting Information.

Ordered nanoparticle assemblies or mesocrystals that extend over several micrometers in the lateral dimensions and about 300 nm in height (Figure 1a–d) have been produced from monodisperse iron oxide nanoparticles by an evaporation-induced self-assembly process. The statistical particle size and size distribution of the synthesized truncated iron oxide nanocubes (Figure 1e, f) have been determined by both TEM and SAXS (see Supporting Information for details). The cubic nanoparticles have an edge length  $l_{\text{SAXS}} = 8.5(1)$  nm with a narrow log-normal size distribution of  $\sigma_{\text{SAXS}} \sim 6\%$  (s.d.). HRTEM images (Figure 1e and Supporting Information) show that the cubes' faces are terminated

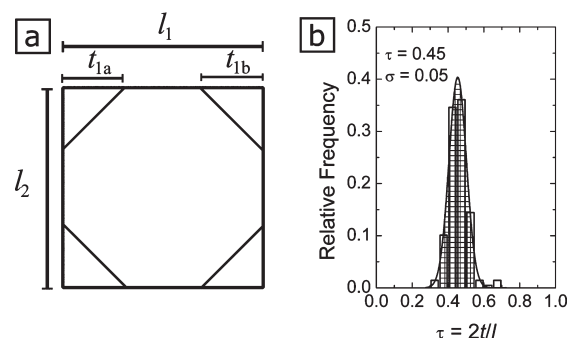


**Figure 2.** Truncation analysis of iron oxide nanocubes. (a) Scheme showing the truncation length,  $t$ , and edge length,  $l$ , for the 2D projection of a truncated cube. (b) Histogram built from the manually measured degrees of truncation,  $\tau$  (bar). The line shows the fit of the histogram with a Gaussian distribution function whereas the hatched area corresponds to  $\tau \pm 2\sigma$ .

on the  $\{100\}$  planes and that both the corners and to a lesser extent the edges are truncated. The corners and edges correspond to the  $\{111\}$  and  $\{110\}$  planes of the spinel structure, respectively. As a measure of the shape anisotropy, the dimensionless degree of truncation,  $\tau_i = 2t_i/l_i$ , is introduced. For comparison,  $\tau = 0$  for an ideal cube, whereas  $\tau = 1$  for a cuboctahedron. The degree of truncation of the nanocubes used in this work was determined by manually measuring the average truncation length,  $t_i = (t_{ia} + t_{ib})/2$ , for each of the cube edges  $l_i$  using HRTEM images at  $800k\times$  magnification, as schematically depicted in Figure 2a. The uncertainty in the determination by TEM of the average value for  $\tau = 2t/l$  can be estimated as

$$\delta\tau = \left[ \left( \frac{\partial\tau}{\partial l} \right)^2 (\delta l)^2 + \left( \frac{\partial\tau}{\partial t} \right)^2 (\delta t)^2 \right]^{1/2} = \left[ \frac{4t^2}{l^4} (\delta l)^2 + \frac{4}{l^4} (\delta t)^2 \right]^{1/2}$$

Above  $600k\times$  magnification, the uncertainties in  $t$  and  $l$  are  $\delta t = 0.145$  nm and  $\delta l = 0.105$  nm, respectively. This yields the

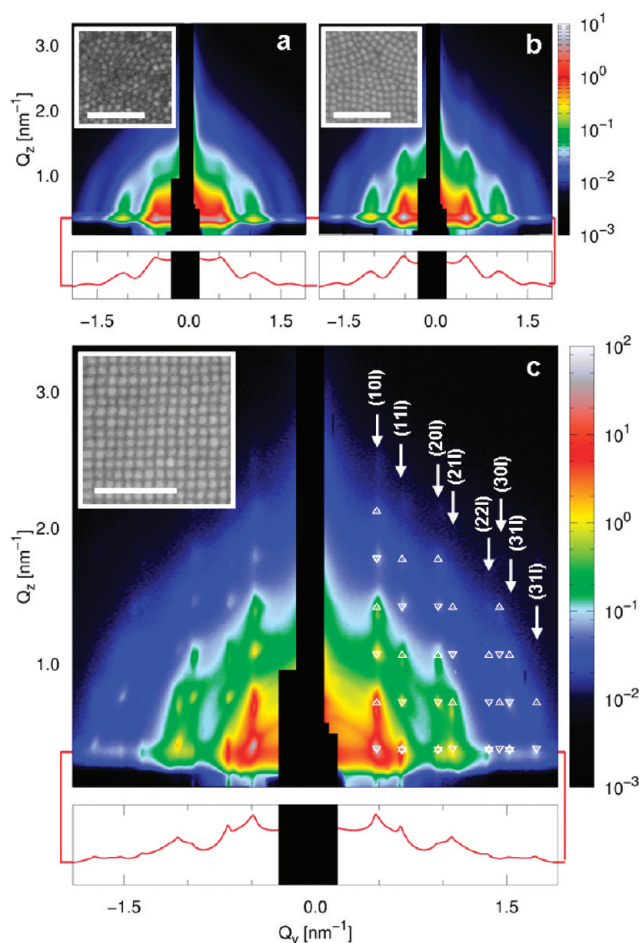


**Figure 3.** GISAXS patterns of assemblies of iron oxide nanocubes. The nanoparticles were allowed to self-assemble onto the Ge substrate under (a) rapid evaporation, (b) slow evaporation, and (c) slow evaporation under a perpendicular magnetic field. *Bct* reflections with (up triangles) and without (down triangles) reflection of the beam at the substrate are indexed. The inserts are representative SEM images of the resulting nanoparticle arrays. Scale bars represent 100 nm. The lateral scattering contributions taken at  $Q_z = 0.34 \text{ nm}^{-1}$  in the respective GISAXS patterns are shown on a logarithmic scale at the bottom.

relatively small maximum uncertainty  $\delta\tau \sim 0.03$  for the measurement. Four values of  $\tau_i$  were obtained from each particle, and the histogram in Figure 2b is constructed from more than 200  $\tau_i$  values. As the figure indicates, a mean value for the degree of truncation,  $\tau = 0.45$  with a standard deviation,  $\sigma_\tau = 0.05$  were obtained from fitting the histogram with a Gaussian distribution function.

Nanoparticle films were deposited on germanium substrates using three different approaches with different evaporation rates and in the absence or presence of an external magnetic field. Spin-coating the wafer with the nanoparticle dispersion allowed the solvent to evaporate in an ambient atmosphere, limiting the time window for self-assembly to a couple of minutes (fast evaporation). The result is a homogeneous albeit disordered monolayer (Figure 3a). This indicates that the time frame before the liquid has evaporated is too short to allow proper rearrangement of the particles while they are still mobile. Prolonging the evaporation time to 1–2 h by allowing the solvent to slowly evaporate in a solvent saturated compartment improved the

long-range order. This is manifested by the formation of a close packed film exhibiting locally ordered domains of square symmetry and a concomitant sharpening of the in plane correlation peaks observed by GISAXS (Figure 3b). Prolonging the evaporation time further by adding a small reservoir of toluene inside the Petri dish did not have a significant effect on the ordering. Application of a weak static magnetic field ( $\sim 30 \text{ mT}$ ) perpendicular to the substrate during the slow evaporation of the nanoparticle dispersion yields highly ordered assemblies of nanocubes in three dimensions (Figure 3c), as opposed to the former methods. This evaporation-induced self-assembly under an external magnetic field results in many three-dimensional mesocrystals that are oriented randomly in the plane of the substrate (Figure 1). The application of a weak magnetic field during the assembly process has been shown to promote the formation of well-ordered mesocrystals of superparamagnetic nanoparticles.<sup>9</sup> Pair interaction energy estimates suggest that the induced dipolar interactions are important for the formation of the initial clusters in solution (see Supporting Information) while the van der Waals interaction dominate in the close packed mesocrystal, as shown below.

Each mesocrystal is internally coherent in terms of structure, which means that the whole sample film (several  $\text{cm}^2$ ) can be treated as a 2D powder with all *hkl* reflections appearing in one GISAXS pattern (Figure 1g). The *hk0* reflections of the in plane symmetry emerge at  $\alpha_f = \alpha_c$ , the critical angle of the particle monolayer, which in this case corresponds to  $Q_z = 0.34 \text{ nm}^{-1}$ . A comparison of the first-order reflections of the lateral scattering contributions at  $Q_y = 0.5 \text{ nm}^{-1}$  yields correlation lengths of 15.8(8) and 17.5(3) nm for the nanocube arrays in panels a and b of Figure 3, respectively. For the magnetically induced arrays in Figure 3c, the correlation length is much larger, exceeding the resolution limit of 65 nm. The very well resolved lateral correlation peaks *hk0* of the nanocube-based superstructures that have self-assembled in the presence of a magnetic field, were indexed according to the square plane group *p4mm* with a lattice constant of  $a = 13.10(5) \text{ nm}$ , in agreement with the observations made by SEM. Five different cubic and tetragonal Bravais lattices can be considered for the 3D mesocrystal structure based on the in plane symmetry obtained from SEM. These are the primitive lattices *sc* and *st*, the body-centered lattices *bcc* and *bct*, and the face-centered lattice *fcc*. The projection of a possible primitive or body-centered unit cell is presented in red in Figure 4, with edge length of  $a = 13.10(5) \text{ nm}$ . For a *bcc* structure, the unit cell body diagonal has to be at least twice as large as the nanoparticle body diagonal. Considering a nanocube edge length of  $l = 8.5(1) \text{ nm}$  and the degree of truncation  $\tau = 0.45$ , the nanocube body diagonal is  $d_{\text{cube}} = 12.5 \text{ nm}$ . With  $a = 13.10(5) \text{ nm}$ , the cubic unit cell diagonal of only 22.7 nm is significantly lower than  $2 d_{\text{cube}}$ , which excludes the *bcc* setting. The centered setting of the plane group indicated in blue in Figure 4 may be imagined as a basis layer for an *fcc* structure. However, with this unit cell orientation the nanocubes are rotated by  $45^\circ$  with respect to the unit cell edges. As a result, a face-centered unit cell that fulfills  $a = b = c$  as required for a cubic symmetry is possible, but the shape and orientation of the nanocubes breaks the cubic symmetry. The rotated nanocubes fulfill neither the 4-fold rotation symmetry in *a* and *b* directions nor the 3-fold rotational symmetry along the unit cell diagonal (see Figure 4b). This structure can thus only be tetragonal rather than cubic, and a face-centered tetragonal symmetry is equivalent to the *bct* structure. For these reasons, an *fcc* lattice is impossible for nanocubes which

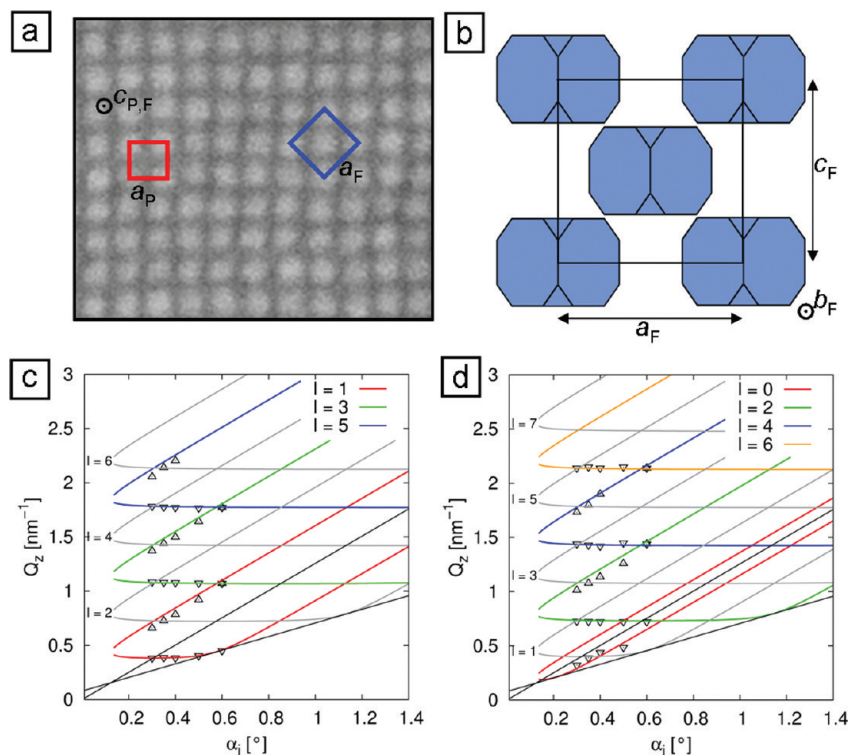


**Figure 4.** Symmetry considerations. (a) Representation of a primitive (red) and a face-centered (blue) unit cell according to the plane group  $p4mm$ . (b) View of a hypothetical face-centered structure in direction of the  $b_F$  lattice constant. The symmetries required for a cubic structure are not obeyed by the nanocubes in this orientation. (c) The  $(10l)$  reflection series and (d) the  $(11l)$  reflection series in  $Q_z$  direction as observed by GISAXS for the nanocube mesocrystals. Theoretical reflection positions according to the incident angle are presented as solid lines.

are laterally ordered in a plane group as compact as found here. Thus, the found plane group is compatible only with  $sc$ ,  $st$ , or  $bct$  lattices. The GISAXS technique finally allows for determination of the full 3D mesocrystal structure. The crystalline stacking order perpendicular to the substrate leads to scattering from lattice planes with  $l \neq 0$ , as can be seen from the reflections above  $\alpha_f = \alpha_c$  in Figure 3c. Those reflections contain a  $z$  component of the scattering vector  $Q$  and the X-ray beam undergoes refraction when it enters and leaves the film. Furthermore, as the incoming or outgoing beam may or may not be reflected at the substrate, the resulting scattering is a set of two signals emanating from a single lattice plane. Assuming a tetragonal lattice for generality, the combination of Snell's and Bragg's laws<sup>29</sup> results in

$$Q_z = k_{i,z} + \sqrt{k_{c,z}^2 + \left[ \sqrt{4\pi^2 \left( \frac{h^2 + k^2}{a^2} + \frac{l^2}{c^2} \right) - Q_y^2} \pm \sqrt{k_{i,z}^2 - k_{c,z}^2} \right]^2} \quad (1)$$

where  $k_{i,z}$  is the  $z$  component of the wave vector of the incoming beam in vacuum,  $k_{c,z}$  is the  $z$  projection of the wave vector at the critical angle, and  $h$ ,  $k$ , and  $l$  are the Miller indices in a tetragonal lattice with the lattice constants  $a$  and  $c$ . The exact  $Q_z$  positions of the GISAXS reflections at different incident angles were determined by Lorentzian fits, and the  $c$  lattice constant and the critical angle of the sample were fitted to the data using eq 1. The refinement of the  $(10l)$  and  $(11l)$  reflection series of the nanocube mesocrystals is shown in panels c and d of Figure 4, respectively. A lattice constant of  $c = 17.80(5)$  nm and a critical angle of refraction of  $0.125^\circ$  were obtained for this sample.

Considering the in plane lattice constant  $a = 13.10(5)$  nm, the observed structure is indeed tetragonal and thus different from the  $sc$  or face-centered cubic ( $fcc$ ) symmetry inferred from electron microscopy. From panels c and d of Figure 4, the extinction rules  $l = 2n + 1$  for  $(10l)$  and  $l = 2n$  for  $(11l)$  reflections can be deduced. In combination with observed extinctions in the  $(20l)$  and  $(21l)$  reflection series, a general extinction rule of  $h + k + l = 2n$  was obtained, leading to the space group  $I4/mmm$  (No. 139) corresponding to a  $bct$  packing of the nanocubes. Thus, with the depth resolution provided by GISAXS we establish for the first time firmly a  $bct$  structure for a nanoparticle mesocrystal.

Colloidal dispersions of hard and soft spheres with dipolar interactions but negligible van der Waals interactions has been found to display a rich phase behavior in the liquid state, including close-packed  $fcc$  and  $hcp$  structures, as well as less dense  $bcc$  and  $bct$  structures.<sup>30,31</sup> According to the phase diagram by Hynninen et al.,<sup>30</sup> the spherical equivalent of our system, with a dipole moment strength  $\gamma \sim 3$  (assuming a magnetically saturated state) and a packing fraction that increases from close to zero in the initial dispersion and upward as the solvent is evaporated, would pass the region of (string) fluid and transverse the  $fcc + \text{fluid}$  and  $fcc$  regions, but not the  $bct$  region, as it dries out. As discussed by Yethiraj et al.,<sup>32</sup> colloidal crystals with  $bct$  symmetry are not close-packed and cannot be preserved upon drying; there is a need to immobilize the dipolar spheres in the liquid state by, e.g., polymerizing a solvent mixture.

The formation of mesocrystals with a  $bct$  structure by an evaporation-induced assembly process appears to be influenced by both the packing constraints of the truncated nanocubes and the anisotropic van der Waals interactions between them. We

**Table 1. Overview of the Number of Nearest Neighbors, Type of Interactions, and Separation Distances in the Experimental *bct* Lattice and a Hypothetical *sc* Lattice<sup>a</sup>**

lattice	fnn			snn			tnn		
	no.	type	distance	no.	type	distance	no.	type	distance
<i>bct</i>	8	corner–corner	$h_0(\tau)$	4	face–face	$h_1 = 4.6 \text{ nm}$	4	edge–edge	$h_2 = 2^{1/2}h_1$
<i>sc</i>	6	face–face	$h_1^{sc} \sim 3.8 \text{ nm}$	12	edge–edge	$h_2^{sc} = 2^{1/2}h_1^{sc}$	8	corner–corner	$h_3^{sc} = 3^{1/2}h_1^{sc} + (2t/3^{1/2})$

<sup>a</sup> fnn, snn, and tnn stand for first-, second-, and third-nearest neighbor.

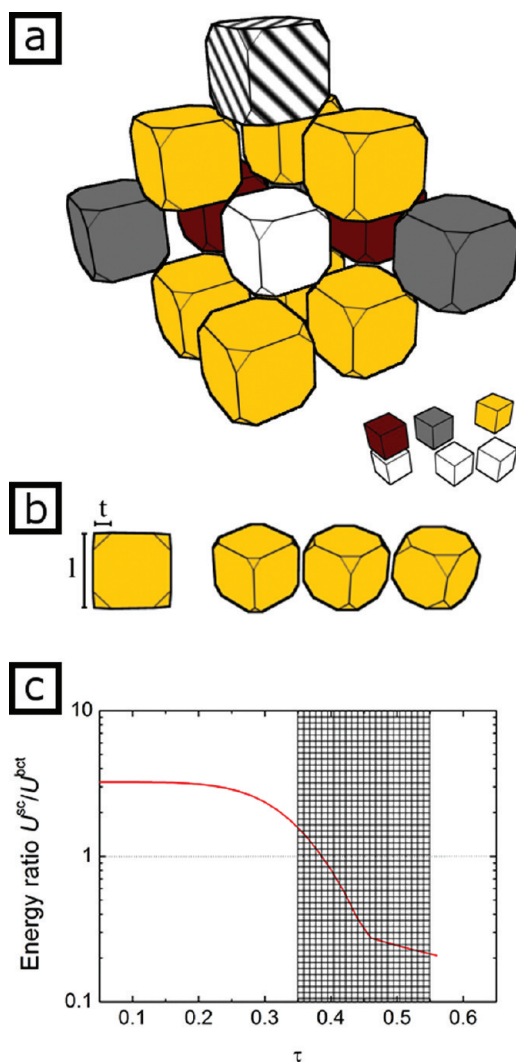


**Figure 5.** Estimation of the interaction energy for simple cubic (*sc*) and body-centered tetragonal (*bct*) arrangements as a function of the degree of truncation. (a) Representation of the *bct* structure type. Particles are colored according to the type of interaction with the white central particle, i.e., face–face, edge–edge, and corner–corner. Particles at distances  $h > 1$  are ignored (e.g., the dashed particle). (b) Visualization of the dimensionless degree of truncation  $\tau$  and representation of nanocubes with variation of  $\tau$ . (c) Ratio between the interaction energies of a truncated cube with an edge length of 8.5 nm in a *bct* and *sc* lattice. The hatched region indicates the degree of truncation investigated in this study.

have made an attempt to model the energy of a particle in a *bct* lattice and compared that to the *sc* lattice. In essence, the model compares the energy required to create a point defect, i.e., to remove a nanocube, in the two structures using both dipolar and

van der Waals (vdW) interactions. The construction of the energetic model of the attractive vdW interactions for such structures requires that the anisotropic interactions arising from the morphology of the truncated cubes are appropriately accounted for.<sup>33</sup> Figure 5a depicts the experimental unit cell and shows the three basic types of interaction, namely, face–face, edge–edge, and corner–corner whereas Table 1 shows the interparticle distances. At moderate truncations ( $0.3 < \tau < 0.58$ ), the interparticle energy for corner–corner interacting particles can be approximated using a variable sphere–sphere approximation that scales geometrically with  $\tau$  (see Supporting Information). Relating the number of nearest neighbors and the separation distances makes it possible to establish a geometrical model that relates the degree of truncation to the total attractive interparticle energy for both structures. Figure 5b shows that at moderate truncation the *bct* configuration dominates over the *sc*, as found experimentally in this work. At low truncations ( $\tau < 0.4$ ), the *sc* structure dominates, thereby predicting a transition from a *sc* to a *bct* structure as the degree of truncation increases.<sup>34</sup> The structural transformation is driven by the rapidly growing vdW attraction along the *bct* diagonal as the degree of truncation increases. This is a consequence of the observation obtained from the analysis of the GISAXS data that the truncated corners approach each other much closer (having as minimum  $h_0 = 0.6 \text{ nm}$ ) compared to the flat faces ( $h_1 \sim 4 \text{ nm}$ ). This short distance found between the truncated corners may be a result of the face-specific adsorption of oleic acid suggesting a surface coverage on the  $\{111\}$  faces that is significantly less than one monolayer. The short distance between the truncated corners and the small lattice constant of  $c = 1.36a$  may also result from shrinkage of the mesocrystal structure perpendicular to the substrate due to residual solvent loss upon final drying of the samples.<sup>20</sup> Alternatively, the interparticle distance in the basal plane of the tetragonal cell, i.e.,  $h_1 = 4.6 \text{ nm}$ , is slightly relaxed compared to that of the *sc* cell ( $h_1^{sc} \sim 3.8 \text{ nm}$ ). The energy expense related to the expansion of the basal plane is compensated by the large vdW corner–corner attraction along the diagonals. Regarding the magnetic dipolar interactions, it is found that, in the case of the *sc* lattice, the multibody dipolar interactions cancel out each other due to the symmetry of the array, whereas in the case of the *bct* lattice, the resulting energy is much smaller than the corresponding vdW energies (see Supporting Information). The estimates of the multibody interaction energies suggest that in the arrays, the additive vdW interactions dominate over the magnetic interactions.

In summary, we have shown that highly ordered body-centered tetragonal mesocrystals with large correlation lengths in three dimensions can be produced by self-assembly of truncated iron oxide nanocubes. The energy modeling, which rests on the detailed structural information obtained primarily from GISAXS together with the well-defined size and degree of truncation of the nanocubes, supports the observations of a *bct*

structure for nanocubes with  $\tau = 0.45$ . This simple model also suggests the formation of a range of structures, such as *sc* and *bct* when the degree of truncation is varied. This work paves the way to a new type of crystallography, where the structure of nanoparticle mesocrystals, the basis of functionality of nanocrystalline assemblies, is largely determined by the shape of the constituents. Improving our understanding of the rich shape-controlled structural diversity of nanoparticle assemblies is of importance in fields ranging from biomineralization to the production of novel functional materials.

## ■ ASSOCIATED CONTENT

**S Supporting Information.** Details on the nanoparticle synthesis, preparation of mesocrystals, further characterization, and van der Waals and dipolar interactions. This material is available free of charge via the Internet at <http://pubs.acs.org>.

## ■ AUTHOR INFORMATION

### Corresponding Author

\*E-mail: [lennart.bergstrom@mmk.su.se](mailto:lennart.bergstrom@mmk.su.se) or [t.brueckel@fz-juelich.de](mailto:t.brueckel@fz-juelich.de).

### Present Addresses

\*Department of Applied Science, University of California, Davis, CA 95616, United States.

### Author Contributions

<sup>†</sup>These authors have contributed equally to this work.

## ■ ACKNOWLEDGMENT

We acknowledge the European Synchrotron Radiation Facility and HASYLAB/DESY for providing the synchrotron radiation facilities and Dr. P. Boesecke and Dr. U. Vainio for support during the GISAXS and SAXS measurements. E.W., G.S.A., and L.B. acknowledge support from the Swedish Research Council (VR). G.S.A. acknowledges partial support from the Wallenberg Wood Science Centre (WWSC). S.D. acknowledges support from the German National Academic Foundation. E. Brauweiler-Reuters is acknowledged for acquisition of the SEM images.

## ■ REFERENCES

- (1) Ozin, G. A.; Arsenault, A. C. *Nanochemistry: A Chemical Approach to Nanomaterials*; The Royal Society of Chemistry: Cambridge, 2005.
- (2) Whitesides, G. M.; Grzybowski, B. *Science* **2002**, *295*, 2418–2421.
- (3) Glotzer, S. C.; Solomon, M. J. *Nat. Mater.* **2007**, *6*, 557–562.
- (4) Murray, C. B.; Kagan, C. R.; Bawendi, M. G. *Annu. Rev. Mater. Sci.* **2000**, *30*, 545–610.
- (5) Laaksonen, A.; Bergström, L. In *Encyclopedia of Complexity and Systems Science*; Meyers, R. A., Ed.; Springer: New York, 2009; pp 7931–7953.
- (6) Bishop, K. J. M.; Wilmer, C. E.; Soh, S.; Grzybowski, B. A. *Small* **2009**, *5*, 1600–1630.
- (7) Whetten, R. L.; Shafiqullin, M. N.; Khoury, J. T.; Schaaff, T. G.; Vezmar, I.; Alvarez, M. M.; Wilkinson, A. *Acc. Chem. Res.* **1999**, *32*, 397–406.
- (8) Talapin, D. V.; Shevchenko, E. V.; Kornowski, A.; Gaponik, N.; Haase, M.; Rogach, A. L.; Weller, H. *Adv. Mater.* **2001**, *13*, 1868.
- (9) Ahnizay, A.; Sakamoto, Y.; Bergström, L. *Proc. Natl. Acad. Sci. U.S.A.* **2007**, *104*, 17570–17574.

- (10) Gupta, S.; Zhang, Q.; Emrick, T.; Russell, T. P. *Nano Lett.* **2006**, *6*, 2066–2069.
- (11) Legrand, J.; Ngo, A. T.; Petit, C.; Pileni, M.-P. *Adv. Mater.* **2001**, *13*, 58–62.
- (12) Zhang, X.; Zhang, Z.; Glotzer, S. C. *J. Phys. Chem. C* **2007**, *111*, 4132–4137.
- (13) Grzelczak, M.; Vermant, J.; Furst, E. M.; Liz-Marzán, L. M. *ACS Nano* **2010**, *4*, 3591–3605.
- (14) Bentzon, M. D.; Wouterghem, J.; van; Mørup, S.; Thölén, A.; Koch, C. J. W. *Philos. Mag. B* **1989**, *60*, 169–178.
- (15) Murray, C. B.; Kagan, C. R.; Bawendi, M. G. *Science* **1995**, *270*, 1335–1338.
- (16) Shevchenko, E. V.; Talapin, D. V.; Kotov, N. A.; O'Brien, S.; Murray, C. B. *Nature* **2006**, *439*, 55–59.
- (17) Shevchenko, E. V.; Talapin, D. V.; Murray, C. B.; O'Brien, S. *J. Am. Chem. Soc.* **2006**, *128*, 3620–3637.
- (18) Chen, J.; Dong, A.; Cai, J.; Ye, X.; Kang, Y.; Kikkawa, J. M.; Murray, C. B. *Nano Lett.* **2010**, *10*, 5103–5108.
- (19) Kalsin, A. M.; Fialkowski, M.; Paszewski, M.; Smoukov, S. K.; Bishop, K. J. M.; Grzybowski, B. A. *Science* **2006**, *312*, 420–424.
- (20) Smith, D. K.; Goodfellow, B.; Smilgies, D.-M.; Korgel, B. A. *J. Am. Chem. Soc.* **2009**, *131*, 3281–3290.
- (21) Quan, Z.; Fang, J. *Nano Today* **2010**, *5*, 390–411.
- (22) Lu, W.; Liu, Q.; Sun, Z.; He, J.; Ezeolu, C.; Fang, J. *J. Am. Chem. Soc.* **2008**, *130*, 6983–6991.
- (23) Saunders, A. E.; Ghezelbash, A.; Smilgies, D.-M.; Sigman, M. B.; Korgel, B. A. *Nano Lett.* **2006**, *6*, 2959–2963.
- (24) Cheon, J.; Kang, N.-J.; Lee, S.-M.; Lee, J.-H.; Yoon, J.-H.; Oh, S. J. *J. Am. Chem. Soc.* **2004**, *126*, 1950–1951.
- (25) Park, J.; An, K.; Hwang, Y.; Park, J.-G.; Noh, H.-J.; Kim, J.-Y.; Park, J.-H.; Hwang, N.-M.; Hyeon, T. *Nat. Mater.* **2004**, *3*, 891–895.
- (26) Rockenberger, J.; Scher, E. C.; Alivisatos, A. P. *J. Am. Chem. Soc.* **1999**, *121*, 11595–11596.
- (27) Salazar-Alvarez, G.; Sort, J.; Suriñach, S.; Baró, M. D.; Nogués, J. *J. Am. Chem. Soc.* **2007**, *129*, 9102–9108.
- (28) Song, Q.; Zhang, Z. *J. Am. Chem. Soc.* **2004**, *126*, 6164–6168.
- (29) Busch, P.; Rauscher, M.; Smilgies, D.-M.; Posselt, D.; Papadakis, C. M. *J. Appl. Crystallogr.* **2006**, *39*, 433–442.
- (30) Hynninen, A.-P.; Dijkstra, M. *Phys. Rev. Lett.* **2005**, *94*, No. 138303.
- (31) Goyal, A.; Hall, C. K.; Velev, O. D. *Phys. Rev. E* **2008**, *77*, No. 031401.
- (32) Yethiraj, A.; Thijsen, J. H. J.; Wouterse, A.; van Blaaderen, A. *Adv. Mater.* **2004**, *16*, 596–600.
- (33) Parsegian, V. A. *Van der Waals forces: a handbook for biologists, chemists, engineers, and physicists*; Cambridge University Press: New York, 2006.
- (34) Demortière, A.; Launois, P.; Goubet, N.; Albouy, P.-A.; Petit, C. *J. Phys. Chem. B* **2008**, *112*, 14583–14592.